5-amino-2-methylpyridinium hydrogen fumarate: an XRD and NMR crystallography analysis

Emily K. Corlett[a], Helen Blade[b], Leslie P. Hughes[b], Philip J. Sidebottom[c], David Walker[a], Richard I. Walton[d] and Steven P. Brown[a]

[a.] *Department of Physics, University of Warwick, Coventry, CV4 7AL*

[b.] *Pharmaceutical Development AstraZeneca, Macclesfield, SK10 2NA*

[c.] *Syngenta, Jealott's Hill International Research Centre, Bracknell, Berkshire, RG42 6EY*

[d.] *Department of Chemistry, University of Warwick, Coventry, CV4 7AL*

Abstract

Single-crystal X-ray diffraction structures of the 5-amino-2-methylpyridinium hydrogen fumarate salt have been solved at 150 and 300 K (CCDC 1952142 and 1952143). A base-acid-base-acid ring is formed through pyridinium-carboxylate and amine-carboxylate hydrogen bonds that hold together chains formed from hydrogen-bonded hydrogen fumarate ions. ^{1}H and ^{13}C chemical shifts as well as ^{14}N shifts that additionally depend on the quadrupolar interaction are determined by experimental magic-angle spinning (MAS) solid-state nuclear magnetic resonance (NMR) and gauge-including projector augmented wave (GIPAW) calculation. Two-dimensional homonuclear ^{1}H-^{1}H double-quantum (DQ) MAS and heteronuclear ^{1}H-^{13}C and ^{14}N-^{1}H spectra are presented. Only small differences of up to 0.1 ppm and 0.6 ppm for ^{1}H and ^{13}C are observed between GIPAW calculations starting with the two structures solved at 150 and 300 K (after geometry optimisation of atomic positions, but not unit cell parameters). A comparison of GIPAW calculated ^{1}H chemical shifts for isolated molecules and the full crystal structures is indicative of hydrogen bonding strength.

Introduction

Salt formation has been common practice within the pharmaceutical industry for more than 25 years[1] as a method of altering the biophysical characteristics of products without altering their pharmacology. An NMR crystallography approach,[2-6] where solid-state NMR and density functional theory (DFT) calculations are employed alongside complementary techniques, is increasingly utilised to characterise the solid form. In the case of crystalline solids, it generally accompanies a structure solution from X-ray diffraction (XRD), providing further insight into the intermolecular interactions and allowing validation and refinement of atomic positions. This is particularly crucial for systems solved from only powder XRD (PXRD) data.

The development of salt systems can be complicated by hydrate formation, as charged ions can interact strongly with polar molecules such as water,[7] which generally leads to instability issues and room temperature phase transitions.[8] Many pharmaceutically acceptable counter ions contain

carboxylate groups which are strongly charged but studies of the Cambridge Structural Database (CSD) show that the incidence of hydrate formation is significantly lower for crystallisations involving pyridine derivatives.[9]

Here we report on the crystallisation of 5-amino-2methylpyridine (52AMP) with fumaric acid (FA), a pharmaceutically acceptable co-former (see Scheme 1). A new salt form, 5-amino-2methylpyridinium hydrogen fumarate (52AMP:F) is reported from single crystal XRD (SXRD) and characterised using a multi-nuclear NMR crystallography approach.

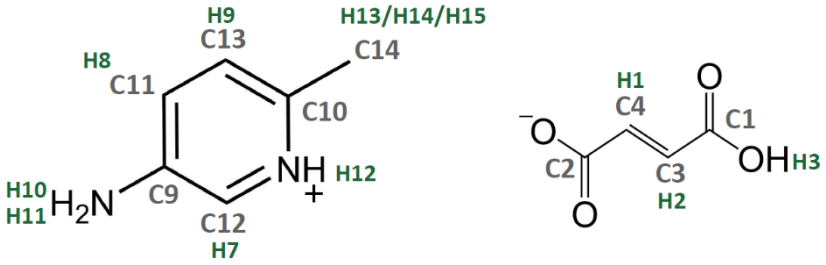

Scheme 1: Molecular structures of 5-amino-2-methylpyridinium (52AMP) and hydrogen fumarate molecules with the atomic labels used in this work.

Experimental details

All chemicals were obtained from Sigma Aldrich (UK) at purities of 98% or higher and used without further purification. 52AMP:F was crystallised by mixing the base (81 mg) and fumaric acid (87 mg) in the minimum amount of hot methanol required to dissolve all the solutes (~ 15 mL) and then allowing the resulting solution to cool slowly at room temperature. Crystals began to form after two days. Crystal growth was improved by co-grinding before dissolution and the addition of seed crystals to subsequent crystallisations.

Crystals were selected for SXRD using polarised light microscopy with an Olympus SZ61 Stereomicroscope. Those that appeared by shape and birefringence to be single crystals were chosen. SXRD was carried out using Cu $K_{\alpha 1}$ (1.5406 Å) on a Rigaku Oxford Diffraction SuperNova diffractometer with an Atlas S2 CCD detector equipped with an Oxford Cryosystems N-Helix cooling system. Crystal screening was conducted at room temperature. CrysAlisPro[10] data-collection and processing software was used, allowing crystals to be checked for quality and giving a preliminary unit cell determination by using a short pre-experiment prior to full data collection. This pre-experiment was also used to screen a minimum of 10 crystals from each crystallisation. Following full data collection, ShelXL[11] was used for structure solution and a least-squares refinement was run, using the Olex2[12] software. Following screening by SXRD, the most crystalline components of each crystallisation were ground to a fine powder and the structure was checked by PXRD to determine bulk purity and ensure no changes had occurred under grinding, by comparing the experimental powder pattern to the pattern predicted from the crystal structure. PXRD was performed on a Panalytical X'Pert Pro MPD equipped

with a curved Ge Johansson monochromator, giving pure Cu $K_{\alpha 1}$ radiation and a solid state PiXcel detector. The powder samples were mounted on a zero-background offcut-Si holder and spun at 30 rpm. Each sample was run with a step size of 0.013° and time per step of 2850 s. A comprehensive analysis of the powder patterns was undertaken using TOPAS Academic v6,[13] which was used for Le Bail[14] and Rietveld[15] refinements.

1D ^{1}H one-pulse, 2D ^{1}H single quantum (SQ) spin-diffusion (NOESY-type), 2D ^{1}H double quantum (DQ) with one rotor period of BaBa recoupling[16, 17] and 2D ^{14}N-^{1}H HMQC[18-21] with R^3 recoupling[22, 23] experiments were performed on a Bruker Avance II+ spectrometer, operating at ^{1}H and ^{14}N Larmor frequencies of 600.0 MHz and 43.4 MHz, respectively, using a 1.3 mm HXY Bruker probe in double resonance mode. A ^{1}H one-pulse MAS spectrum was acquired with 8 coadded transients using a recycle delay of 80 s (this recycle delay was sufficient to ensure that the signal had plateaued). Each 2D fast MAS experiment employed a rotor synchronised t_1 increment of 16.67 μs and was acquired with 8 coadded transients for each of 128 t_1 FIDs using a recycle delay of 80 s, corresponding to an experimental time of 23 hours. 133 μs of R^3 recoupling was employed for the 2D ^{14}N-^{1}H HMQC. The spin-diffusion spectrum was collected with a mixing time of 1 s.

1D ^{1}H-^{13}C cross-polarisation (CP) MAS and 2D ^{1}H-^{13}C heteronuclear correlation (HETCOR) experiments were performed on a Bruker Avance III spectrometer, operating at ^{1}H and ^{13}C Larmor frequencies of 500.0 MHz and 125.8 MHz, respectively, using a 3.2 mm HX probe. A ^{13}C CP MAS spectrum was acquired with 16 coadded transients, a CP contact time of 1500 μs and a recycle delay of 80 s. A 2D ^{1}H-^{13}C HETCOR spectrum was acquired with 24 transients coadded for each of 120 t_1 FIDs using a recycle delay of 80 s, a t_1 increment of 36 μs and a CP contact time of 500 μs (corresponding to a total experiment time of 64 hrs). eDUMBO-1_{22}[24, 25] homonuclear decoupling was used with a 32 μs cycle, with 320 divisions of 100 ns each. The scaling factor was determined to be 1.6. In the HETCOR pulse sequence, the following phase cycling was employed: ^{1}H 90° pulse (90º 270°), ^{13}C CP contact pulse (2{0°} 2{180°} 2{90°} 2{270°}), receiver (0° 180° 180° 0° 90° 270° 270° 90°). For both CP MAS and HETCOR ^{1}H-^{13}C experiments, SPINAL64[26] ^{1}H heteronuclear decoupling was applied during the acquisition of the ^{13}C FID, with a pulse duration of 5.9 μs at a nutation frequency of 100 kHz, and a 70 to 100% ramp[27] on the ^{1}H channel was used for the CP contact time with nutation frequencies of 47.5 and 60 kHz for ^{13}C and ^{1}H, respectively. In all cases (except during CP), a ^{1}H nutation frequency of 100 kHz was used corresponding to a ^{1}H 90° pulse duration of 2.5 μs.

^{13}C and ^{1}H chemical shifts are referenced with respect to tetramethylsilane (TMS) via L-alanine at natural abundance as a secondary reference (1.1 ppm for the CH_3 ^{1}H resonance and 177.8 ppm for the CO ^{13}C resonance) corresponding to adamantane at 1.85 ppm (^{1}H)[28] and 38.5 ppm (^{13}C)[29]. ^{14}N shifts are referenced with respect to a saturated NH_4Cl aqueous solution via spectra of L-β-aspartyl-L-alanine at natural abundance (−284 ppm for the lower NH resonance at a Larmor frequency of 43.4 MHz) corresponding to liquid CH_3NO_2 at 0 ppm.[20, 30] ^{1}H, ^{13}C and ^{14}N shifts can be experimentally determined to an accuracy of ± 0.2, ± 0.1 and ± 5 ppm, respectively.

Density functional theory (DFT) calculations were performed using CASTEP[31] Academic Release version 16.1. All calculations used the Perdew Burke Ernzerhof (PBE) exchange correlation functional,[32] a plane-wave basis set with ultrasoft pseudopotentials and a plane-wave cut-off energy of 700 eV. Integrals over the Brillouin zone were taken using a Monkhorst-Pack grid of minimum sample spacing 0.1 × 2π $Å^{-1}$ (unless otherwise stated). Geometry optimisation was performed (all atoms were allowed to move) on both the 150 K and 300 K structures with the unit cell parameters fixed to the values determined by diffraction at the specific temperature. Note that the numbering used in this paper (see Scheme 1) follows from the CASTEP calculation where hydrogen and carbon atoms for the two equivalent (Z = 2) hydrogen fumarate ions are listed first (*i.e.*, positions C5 to C8 and H4 and H6 are equivalent to C1 to C4 and H1 to H3).

NMR parameters were calculated using the gauge-including projector-augmented wave (GIPAW)[33] method and were performed for both the geometry optimised crystal structures as a whole and for each of the isolated molecules in the asymmetric unit. For the isolated molecule calculations, each molecule in the asymmetric unit was extracted from the geometry optimised unit cell and placed in a sufficiently large box such that it could not interact with repeated molecules across periodic boundary conditions[34] (unit cell dimensions increased by 10 Å in each direction). As each individual molecule carried a charge, this was specified in the .param file.[35]

The calculated isotropic chemical shifts (δ_{iso}^{calc}) were determined from the calculated chemical shieldings (σ_{calc}) by $\delta_{iso}^{calc} = \sigma_{ref} - \sigma_{calc}$, with calculated σ_{ref} values of 30.0 and 170.8 ppm for ^{1}H and ^{13}C, respectively. σ_{ref} was determined for ^{1}H and ^{13}C by taking the sum of the experimental chemical shift and the GIPAW calculated absolute isotropic chemical shieldings. The resulting y-intercept was taken as σ_{ref}.[36, 37] A literature value of −153 ppm was used for ^{14}N.[38] It is noted that it is common practice to calculate a specific reference shielding for each system[39], though average values over a range of compounds are also available.[40] By comparing the parameters in the full crystal structure with those for the isolated molecule, insight is provided into the intermolecular interactions responsible for maintaining the crystal structure.[41]

Results and Discussion

XRD

The crystal structure of 52AMP:F has been determined, as described below, at both 150 K and 300 K and the structures deposited with the CCDC, no. 1952142 and 1952143, respectively. Selected crystal data for the structure at each temperature are given in Table 1. A small thermal expansion occurred on heating from 150 K to 300 K but with no evident change in the molecular packing. Hydrogen atoms were found in the electron density map. Initial verification of proton transfer was completed by

comparison of the carboxylate C-O bond lengths and was then confirmed by ^{14}N-^{1}H HMQC NMR experiments, as discussed below.

Table 1: Selected crystal data for 52AMP:F for structures determined at both 150 K and 300 K

Stoichiometry (base : acid)	1 : 1	1 : 1
Chemical formula	$C_{10}H_{12}N_2O_4$	$C_{10}H_{12}N_2O_4$
Formula weight (g mol^{-1})	224.22	224.22
Crystal system	Triclinic	Triclinic
Space group	$P\bar{1}$	$P\bar{1}$
***a* (Å)**	8.0467(3)	8.0482(6)
***b* (Å)**	8.0181(3)	8.1802(6)
***c* (Å)**	9.3998(3)	9.5519(6)
***α* (°)**	109.263(3)	110.893(7)
***β* (°)**	93.715(3)	92.764(6)
***γ* (°)**	110.974(3)	111.438(7)
Z	2	2
Temperature (K)	150	300
***R*1 [$I > 2\sigma(I)$]**	0.0354	0.0435

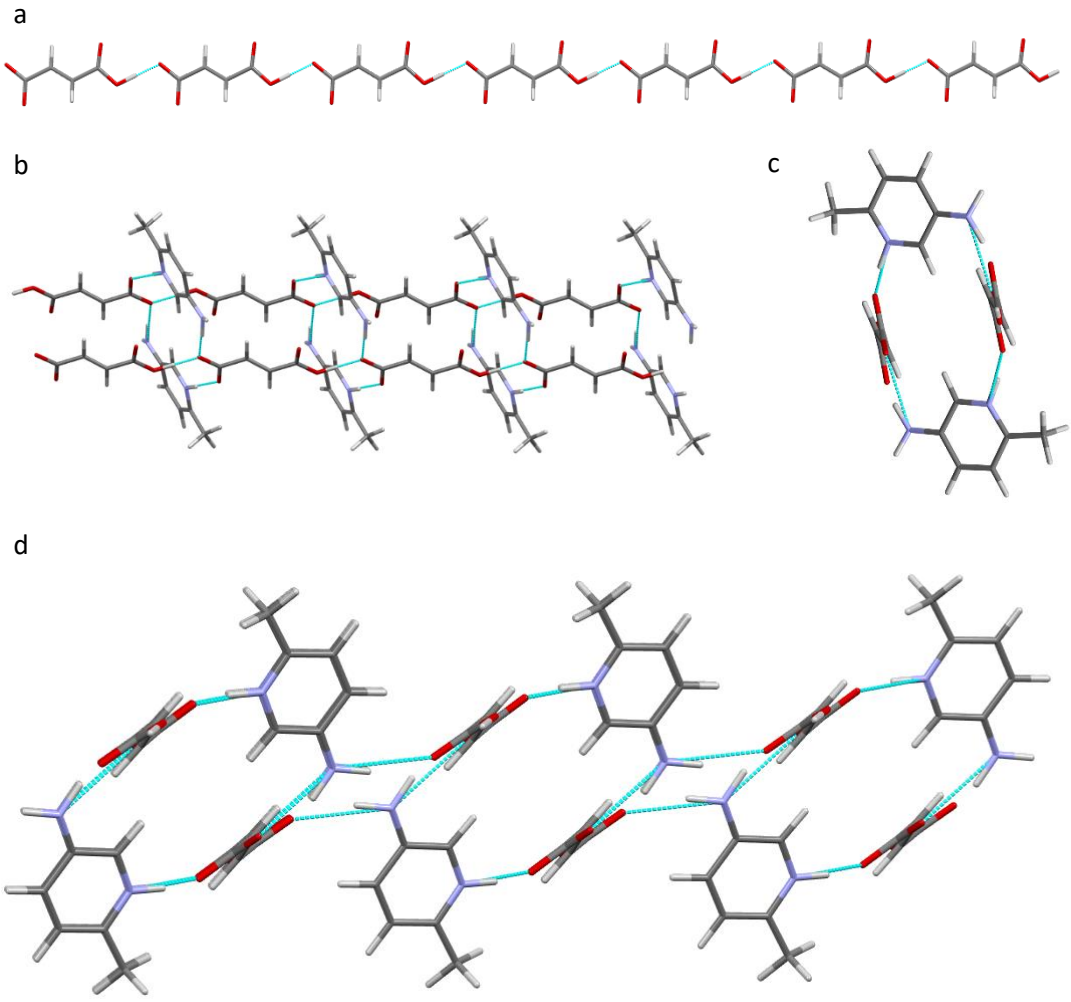

Figure 1: Packing of 52AMP:F showing (a) the acid chain, the paired acid chains linked through the 52AMP molecules viewed (b) along the c *axis and (c) along the* a *axis, and (d) a set of paired chains joined into the smaller ring motif.*

52AMP:F has a stoichiometry of 1 : 1, base : acid, and crystallises in the triclinic space group $P\bar{1}$. Hydrogen fumarate molecules form acid chains along the a-axis with graph set notation $C_1^1(7)$ (Fig.

1a).[42] These chain structures, with a base ion hydrogen bonded to the carboxylate group of each hydrogen fumarate, are directly analogous to the chain structures seen in 2,6-lutidinium hydrogen fumarate.[43, 44] Pairs of these chains, running in opposite directions, are linked through the 52AMP ions associated with each hydrogen fumarate (Fig. 1b). Through pyridinium-carboxylate and amine-carboxylate H-bonds, a base-acid-base-acid ring is formed, $R_4^4(18)$, which supports this pairing (Fig. 1c).[42] A H-bond via the other amino proton, to the carboxylic acid O=C, allows crosslinking between paired chains, forming a H-bonded layer on the (010) crystal plane (Fig. 1d). These layers then stack to form the 3D structure. Neither fumaric acid nor doubly ionised fumarate are present, with the occurrence of hydrogen fumarate instead preventing the formation of the base-acid-base units seen in other related systems, such as Bis-(2-amino-5-methylpyridinium) fumarate fumaric acid.[45, 46] The H-bond parameters at 300 K for the significant H-bonding motifs identified are given in Table 2.

PXRD of 52AMP:F showed no evident change in structure on grinding (SI, Fig. S1). A Rietveld refinement of the experimental powder pattern against the SXRD structure gave R_{wp} = 8.59% and R_{Bragg} = 1.24% (SI, Tables S1 and S2).

Table 2: Selected structural parameters for 52AMP:F at 150 K (following geometry optimisation).

N···O distance (Å)	**$NH^+\cdots^-O$ angle (°)**	**NH···O angle (°)**	**O···O distance (Å)**	**OH···O angle (°)**
2.65	160.4	-		
2.92	-	160.1		
2.98	-	163.3		
			2.50	178.1

NMR

Fig. 2 shows 1D ^{1}H MAS and ^{1}H-^{13}C CP MAS spectra for 52AMP:F. Assignments are based on both the GIPAW calculated chemical shifts (Tables 3 and 4) and the 2D MAS NMR spectra, discussed in detail below. It is interesting to note that, despite the noticeable thermal expansion of the unit cell between 150 K and 300 K (Table 1), any changes in interatomic distances are too small to result in significant changes in the GIPAW calculated chemical shifts, with differences limited to 0.1 ppm and 0.6 ppm for ^{1}H and ^{13}C, respectively.

52AMP:F show good agreement for ^{1}H between experimental NMR chemical shifts and calculated GIPAW chemical shifts. Surprisingly, as no indication was seen in the PXRD pattern in Fig. S1, the ^{1}H MAS spectrum for 52AMP:F has a resonance thought to correspond to crystalline fumaric acid at 12.8 ppm (Fig. 2) as seen previously for 2,6-lutidinium hydrogen fumarate.[44] Other than this minor secondary phase, the only discrepancy for 52AMP:F (the established discrepancy between GIPAW calculations and experimental values is only around 1% of the chemical shift range, ~ 0.2 ppm for ^{1}H) corresponds to the apparent overcalculation of H3, the OH proton involved in an OH···O H-bond, which experimentally is 1.6 ppm lower than the calculated value (δ_{iso}^{calc} = 18.4 ppm compared to

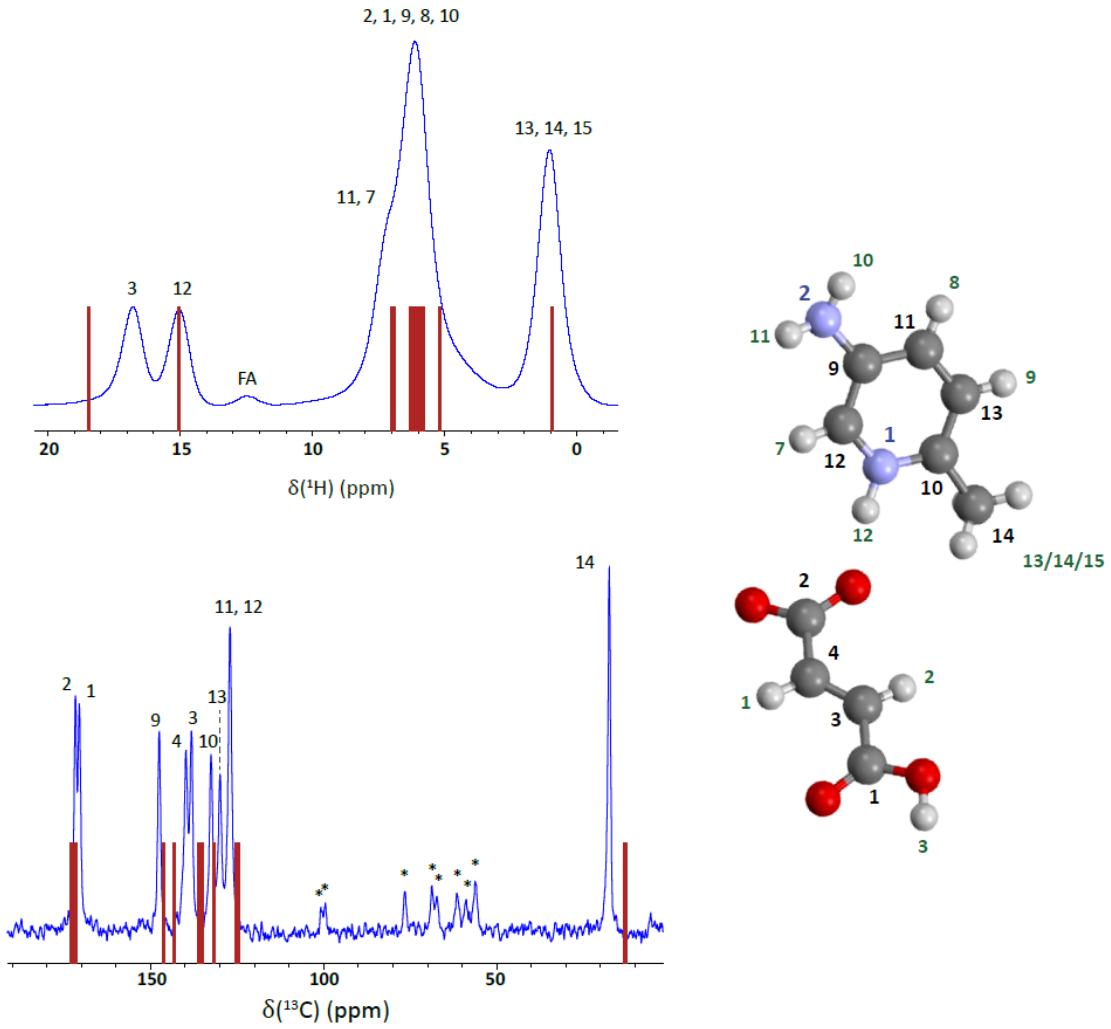

Figure 2: ^{1}H (600 MHz) one-pulse MAS (60 kHz) and ^{1}H-^{13}C CP-MAS (12.5 kHz) spectra of 52AMP:F (top and bottom, respectively) with stick spectra corresponding to GIPAW calculated chemical shifts. The assignments to each atom, as labelled in the structure on the right, are given.

δ_{iso}^{exp} = 16.8 ppm). This is the same environment for which a larger than anticipated discrepancy was previously described for 2,6-lutidine hydrogen fumarate.[44]

Despite the excellent agreement seen for the ^{1}H chemical shifts for 52AMP:F, there is relatively poor agreement for the ^{13}C chemical shifts. The 1% rule of thumb stated above gives expected error between GIPAW calculations and experimental values of up to ~2 ppm for ^{13}C. It can be clearly seen in the 1D ^{1}H-^{13}C CP MAS spectrum in Fig. 2 that this is exceeded for numerous carbon environments in 52AMP:F. For the highest and lowest chemical shifts, as usual, GIPAW calculation underestimates and overestimates the low ppm and high ppm values, respectively. In addition, while C10 is calculated to lie 2.8 ppm lower than it is seen experimentally, both C3 and C4 are calculated to lie more than 3 ppm higher than their experimental chemical shifts. These latter two are the CH carbons in the hydrogen fumarate anion.

Fig. 3a shows that there are clear correlations in the ^{1}H-^{1}H DQ MAS spectrum of 52AMP:F for H12 (NH) with H3 (OH), H7 (aromatic CH) and the methyl group at δ_{DQ} = 15.0 + 16.8/7.1/1.0 = 31.8/22.1/16.0 ppm. The low intensity resonances that appear as shoulders on the pair of H12-H7 cross-

Table 4: GIPAW calculated and experimental ^{1}H chemical shifts

		δ^{iso}_{calc}(^{1}H) (ppm)		δ_{exp} (^{1}H) (ppm)
	Atom	**150 K**	**300 K**	
Me	H13/H14/H15	0.9	0.9	1.0
CH	H8	5.8	5.9	6.1
	H9	6.0	5.9	6.1
	H1	6.2	6.2	6.1
	H2	6.3	6.3	6.1
	H7	6.9	6.8	7.1
NH_2	H10	5.2	5.1	6.1
	H11	7.0	7.1	7.1
NH	H12	15.1	15.2	15.0
OH	H3	18.4	18.4	16.8

Table 3: GIPAW calculated and experimental ^{13}C chemical shifts

		δ^{iso}_{calc}(^{13}C) (ppm)		δ_{exp} (^{13}C) (ppm)
	Atom	**150 K**	**300 K**	
Me	C14	12.9	12.9	17.4
CH/C	C12	124.5	124.6	127.0
	C11	125.4	125.1	127.0
	C13	131.7	131.3	129.9
	C10	135.4	135.6	138.2
	C3	135.9	136.3	132.5
	C4	143.4	142.8	139.7
	C9	146.3	146.4	147.5
$COOH/^{-}$	C1	172.7	172.7	170.6
	C2	173.2	173.2	171.7

peaks are thought to correspond to the H12-H9 proximity (δ_{DQ} = 15.0 + 6.1 = 21.1 ppm). The H12-H9 correlation is expected to be weaker as H9 is significantly further away at 3.38 Å as compared to 2.71 Å for H3 (see Table 5). A 2D SQ ^{1}H-^{1}H NOESY spectrum (Fig. 3b) was used to confirm the presence of fumaric acid as it shows the existence of two distinct phases. A mixing time of 500 ms was used to allow spin diffusion throughout the entirety of each phase,[47, 48] with the clear separation of cross-peaks indicating the occurrence of more than one phase. Only a single correlation was seen for the resonance at δ^{exp} = 12.8 ppm, corresponding to a proximity to a proton with a chemical shift in the CH region, as

expected for the OH proton of crystalline fumaric acid. The relatively low ratio of fumaric acid within the sample is evidenced by the lack of DQ correlations (evident at the selected base contour level) for the fumaric acid peak in the ^{1}H-^{1}H DQ MAS spectrum.

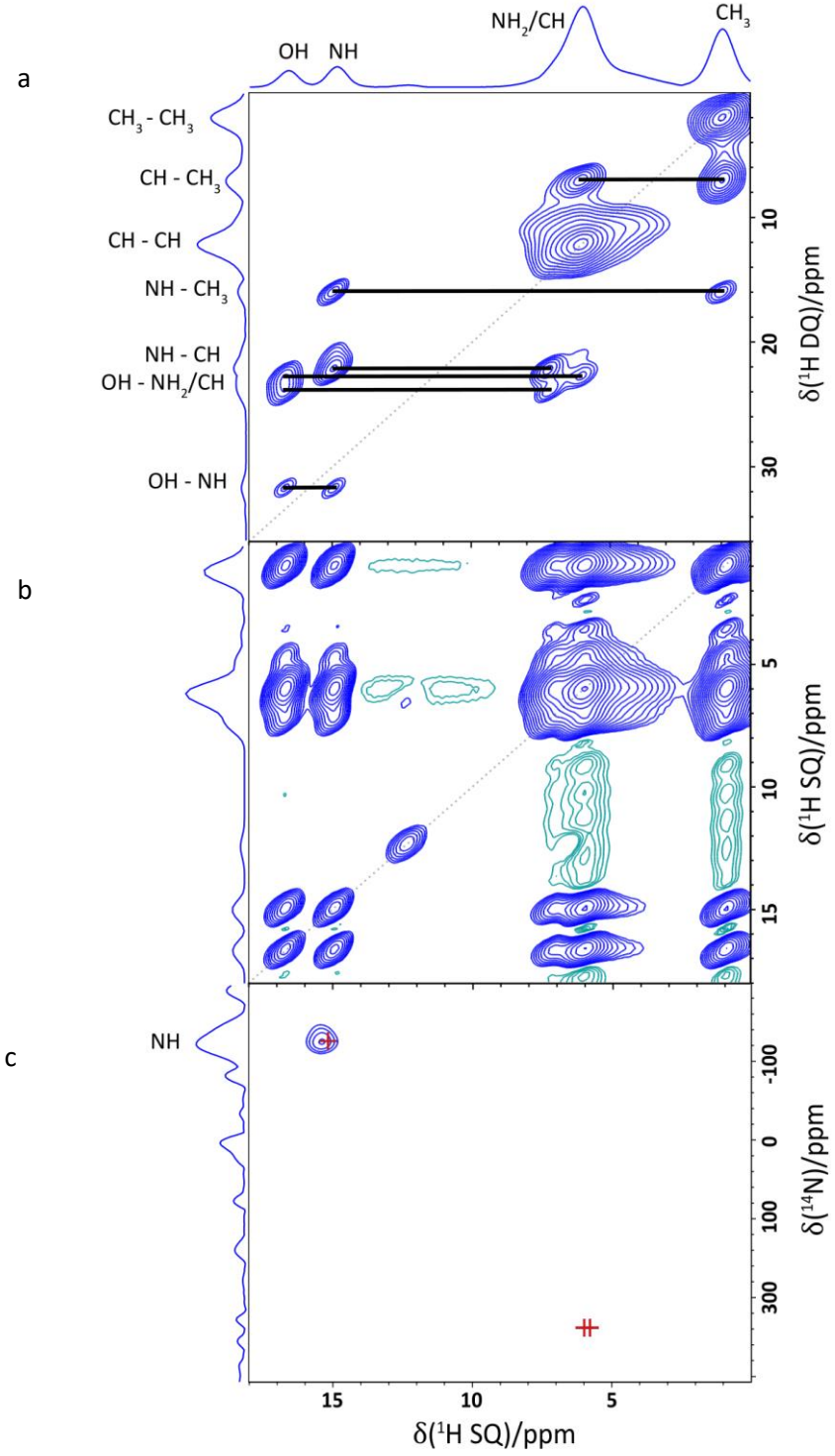

Figure 3: 2D MAS (60 kHz) NMR spectra of 52AMP:F. (a) a ^{1}H-^{1}H DQ spectrum recorded with one rotor period of BaBa recoupling; (b) a ^{1}H-^{1}H SQ NOESY spectrum with t_{mix} = 500 ms; and (c) a ^{14}N-^{1}H HMQC spectrum with 8 rotor periods of R^{3} recoupling, with GIPAW calculated chemical shifts for N···H proximities < 2 Å shown as red crosses. All spectra were recorded at a ^{1}H Larmor frequency of 600 MHz. Base contour levels are at 8.4%, 1.5% and 40.1% of the maximum peak height, respectively. Blue and green contours correspond to positive and negative intensity, respectively. The negative intensities seen at the CH_3 and CH F_1 (vertical axis) SQ frequencies in (b) are due to the much greater intensity of their auto-correlation peaks. The dashed diagonal lines in (a) and (b) indicate the (a) $\delta_{DQ} = 2\delta_{SQ}$ and (b) $\delta_{SQ} = \delta_{SQ}$ diagonals.

Table 5: H···H proximities (<3.5 Å) and corresponding ^{1}H DQ chemical shifts for the pyridine NH and the OH of 52AMP:F

NH	δ_{iso}^{exp} SQ1 (ppm)	Proton 2	δ_{iso}^{exp} SQ2 (ppm)	δ_{iso}^{exp} DQ (ppm)	Separation[a] (Å)
H12 (NH)	15.0	H7	7.1	22.1	2.31
		H13/H14/H15	1.0	16.0	2.35
		H3	*16.8*	*31.8*	*2.71*
		H9	*6.1*	*21.1*	*3.38*
H3 (OH)	16.8	H2	*6.1*	*22.9*	*2.78*
		H8	*6.1*	*22.9*	*2.93*
		H7	*7.1*	*23.9*	*2.93*
		H11	*7.1*	*23.9*	*2.94*

[a] H-H distances are taken from the DFT (CASTEP) optimised structure. Intermolecular proximities are denoted using italic font.

A ^{14}N-^{1}H HMQC spectrum of 52AMP:F (Fig. 3c) does not show any cross-peaks for the NH_2 protons but confirms the assignment of the NH (H12) ^{1}H resonance, with the calculated ^{14}N chemical shift and quadrupolar parameters being consistent with proton transfer in the salt form ($\delta^{exp} = -126.1$ ppm, $\delta^{calc} = -126.6$ ppm, see SI, Table S3). The absence of the NH_2 correlation is likely due to the difference in build-up of the recoupled signal between nitrogen environments, with the NH_2 signal already decaying before the NH signal reaches its maximum.

A 2D ^{1}H-^{13}C HETCOR MAS NMR spectrum of 52AMP:F is shown in Fig. 4, recorded using a CP contact time of 500 μs such that cross-peaks for longer-range C···H proximities are apparent as well as direct one-bond C-H connectivities. The ^{1}H-^{13}C HETCOR spectrum is shown together with crosses that represent the GIPAW calculated chemical shifts for the C-H dipolar correlations up to 3.3 Å (see Table S4 in the SI). More correlations with the methyl protons are present experimentally than expected for this cut off distance, with small cross-peaks apparent for C3 (δ^{exp} = 132.5 ppm, δ^{calc} = 135.9 ppm), C9 (δ^{exp} = 147.5 ppm, δ^{calc} = 146.3 ppm) and C1 (δ^{exp} = 170.6 ppm, δ^{calc} = 172.7) which have methyl proton proximities of 3.51 Å (C3 and C9) and 3.40 Å (C1). Crosses for the GIPAW calculated chemical shifts for such long-range proximities (>3.3 Å) were not included as they are not seen experimentally for any other proton environments.

The aforementioned disparities between experiment and calculation for the ^{13}C chemical shifts mean that C10 and C3 are seen experimentally in the opposite order to which they are calculated. Their calculated ^{13}C chemical shifts lie only 0.4 ppm apart with C10 at the lower chemical shift. The assignment of C10 to the resonance at δ^{exp} = 138.2 ppm is, however, confirmed by its cross-peak with H12 at δ^{exp} = 15.0 ppm, with a C10-H12 proximity of 2.08 Å compared to a distance of 3.68 Å for C3-

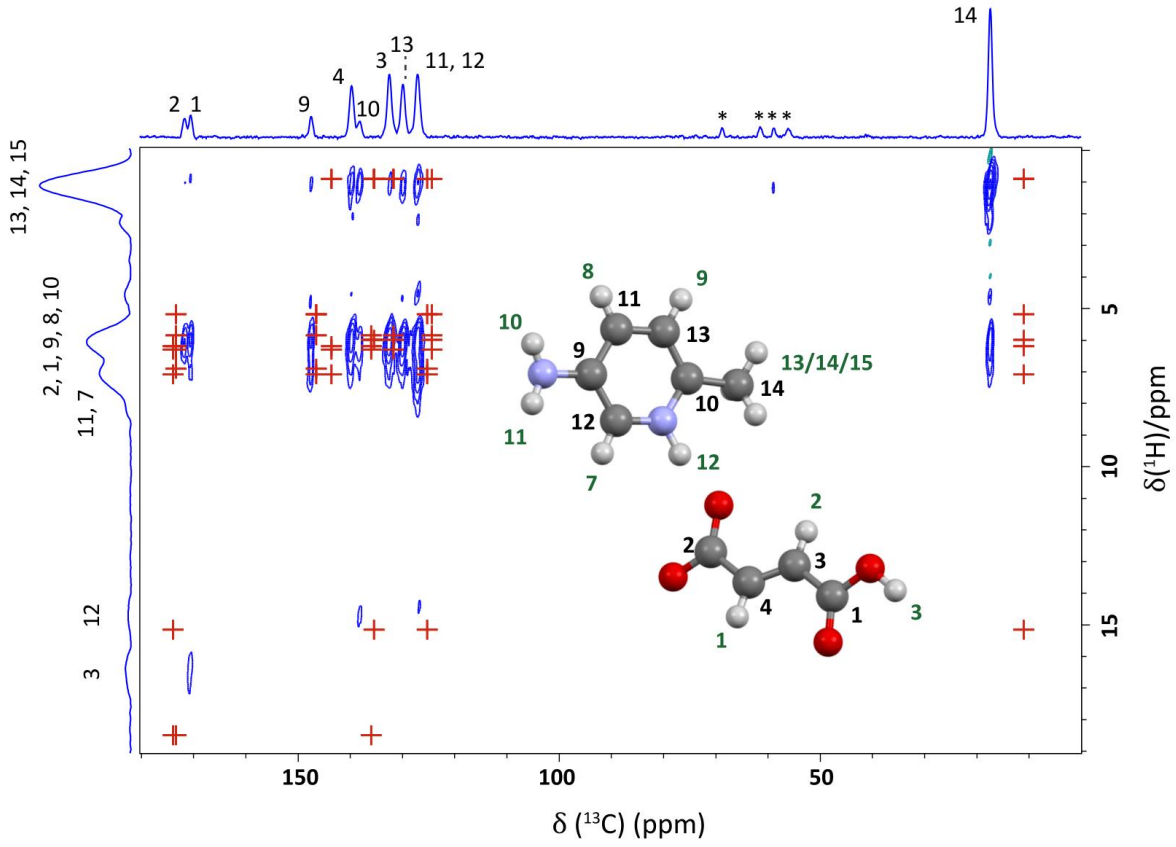

Figure 4: A ^{1}H (700 MHz)-^{13}C CP (500 μs) HETCOR MAS (12.5 kHz) NMR spectrum of 52AMP:F recorded using FSLG ^{1}H homonuclear decoupling in t_1. GIPAW calculated chemical shifts are shown as red crosses for C···H proximities < 3.3 Å. The base contour level is at 4.9% of the maximum peak height.

H12. The H12 cross-peak for the ^{13}C resonance at δ^{exp} = 127.0 ppm also confirms that C12 lies under this peak along with C11. Correlations are missing for C2-H12, C2-H3, C3-H3 and C14-H12. The former two carbons are quarternary so this is not surprising, despite the relevant distances for C2 being significantly shorter than for other correlations present at 2.30 Å and 2.68 Å for H12 and H3, respectively. The absence of the C3-H3 cross-peak is expected as not only is C3 quaternary, but this corresponding distance is 3.29 Å, on the limit of what is seen for any other carbon environment. The absence of the C14-H12 cross-peak is rather more inexplicable as this is a methyl carbon and the C-H separation is 2.60 Å.

Intermolecular interactions

Comparing the GIPAW chemical shifts calculated for the entire crystal structure to those calculated for individual isolated molecules, as extracted from the geometry optimised crystal structure, is useful as significant differences between the two indicate the presence of intermolecular interactions.[34, 41, 49-52] For ^{1}H, changes are considered significant for $\Delta\delta_{Cryst\text{-}Mol}$ exceeding 1 ppm. The isolated molecule calculations for 52AMP:F identify only the four classical H-bonds (Table 6) that were assumed from proximities and angles within the crystal structure (Table 2). The OH···O interaction involving H3 is by far the strongest with $\Delta\delta_{Cryst\text{-}Mol}$ = 11.9 ppm and corresponding to both the shortest distance, at 2.50

Table 6: A comparison of GIPAW calculated ^{1}H shifts (in ppm) for the full geometry optimised crystal structure of 52AMP:F and isolated molecules extracted from the geometry optimised crystal structure.

Atom	δ_{Expt}	$\delta_{Crystal}$	$\delta_{Molecule}$	$\Delta\delta_{Crystal\ -\ Molecule}$
H3	16.8	18.4	6.5	11.9
H12	15.0	15.1	9.6	5.5
H11	7.1	7.0	4.0	3.0
H10	6.1	5.2	3.9	1.3
H7	7.1	6.9	6.4	0.5
H2	6.1	6.3	6.0	0.3
H1	6.1	6.2	6.1	0.1
H9	6.1	6.0	6.5	–0.5
H8	6.1	5.8	6.5	–0.7
H13/H14/H15	1.0	0.9	1.63	–0.7

Å, and the most linear bond, with an OHO angle of 178.1°. This is followed in strength by the pyridinium $NH^{+}\cdots^{-}O$ at $\Delta\delta_{Cryst\text{-}Mol}$ = 5.5 ppm, which is the next shortest. Even allowing for the over estimation of OH···O ^{1}H chemical shifts (discussed above), this $\Delta\delta_{Cryst\text{-}Mol}$ value is still nearly twice as large as that for the pyridinium interaction. The other two significant interactions correspond to the amino NH···O H-bonds which are both weaker than the pyridinum H-bond with one (H10, which forms cross-links between paired acid chains) substantially so, only forming a H-bond with $\Delta\delta_{Cryst\text{-}Mol}$ = 1.3 ppm. Even the more tightly bound amino NH H-bond (for H11) only has $\Delta\delta_{Cryst\text{-}Mol}$ = 3.0 ppm. H11 corresponds to a marginally shorter N···O distance of 2.92 Å, compared to a distance of 2.98 Å for the H10 H-bond, which results in a stronger interaction despite the NHO angle being slightly less linear at 160.1°, compared to 163.3° for the H10 H-bond.

Conclusions

The crystallisation of 5-amino-2-methylpyridine with fumaric acid results in a 1:1 salt, 52AMP:F, the structure of which was solved by SXRD. The molecular packing is based upon a hydrogen fumarate acid chain akin to that seen for 2,6-lutidinium hydrogen fumarate.[43] PXRD was utilised to confirm the composition of the bulk prior to analysis by solid-state NMR.

As well as exhibiting similar structural patterns as the 2,6-lutidinium salt, the OH···O interaction was also found to show a comparable discrepancy between the experimental and GIPAW calculated chemical shifts, with the hydrogen bonded proton calculated 1.6 ppm higher than observed experimentally for 52AMP:F (a difference of 1.9 ppm was recorded for 2,6-lutidinium hydrogen fumarate).[44] Excluding this one exceptional proton, there was excellent agreement between GIPAW calculated and the experimentally observed resonances of both ^{1}H chemical shifts and pyridinium ^{14}N shift. The errors for the ^{13}C chemical shifts were slightly higher than expected difference of ~2 ppm, with the largest difference (excluding the methyl carbon which differs due to temperature effects) being

−3.7 ppm, although the average absolute error still only 2.5 ppm. There is no obvious cause for this level of variation and no significant difference in it between calculations performed for the 150 K and 300 K structures, which differ only by a small thermal expansion.

The key intermolecular interactions supporting the structure were confirmed, by the isolated molecule GIPAW NMR chemical shift calculations, to consist of only four classical hydrogen bonds expected from analysis of the crystal structure, with no CH donors or π interactions apparent. The H-bond strength, according to the change in calculated chemical shift between crystal and isolated molecule, matched that expected from the hydrogen bond parameters. The relative strength of the two weaker NH···O hydrogen bonding interactions, formed by each of the two NH_2 protons, also implies that a slight lengthening of the hydrogen bond has a larger impact on hydrogen bonding strength than a small change in NH…O angle further from linearity.

Acknowledgments

We thank Dr Guy Clarkson for his assistance with the SXRD analysis. Emily Corlett thanks EPSRC, AstraZeneca and Syngenta for a PhD studentship through the EPSRC Centre for Doctoral Training in Molecular Analytical Science, grant number EP/L015307/1. Crystallographic data were collected using an instrument that received funding from the European Research Council (ERC) under the European Union's Horizon 2020 research and innovation programme (grant agreement No 637313, PI: Adrian Chaplin, Chemistry, University of Warwick). Some of the equipment used in this work was provided by the University of Warwick's Research Technology Platforms

The calculated and experimental data for this study are provided as a supporting data set from WRAP, the Warwick Research Archive Portal at http://wrap.warwick.ac.uk/***.

References

1. S. M. Berge, L. D. Bighley and D. C. Monkhouse, *J. Pharm. Sci.*, 1977, **66**, 1-19.
2. S. E. Ashbrook and D. McKay, *Chem. Commun.*, 2016, **52**, 7186-7204.
3. B. Elena, G. Pintacuda, N. Mifsud and L. Emsley, *J. Am. Chem. Soc.*, 2006, **128**, 9555-9560.
4. R. K. Harris, *Solid State Sci.*, 2004, **6**, 1025-1037.
5. C. Bonhomme, C. Gervais, F. Babonneau, C. Coelho, F. Pourpoint, T. Azais, S. Ashbrook, J. Griffin, J. Yates, F. Mauri and C. Pickard, *Chem. Rev.*, 2012, **112**, 5733-5779.
6. T. Charpentier, *Solid State Nucl. Magn. Reson.*, 2011, **40**, 1-20.
7. A. Trask, W. Motherwell and W. Jones, *Crystal Growth & Design*, 2005, **5**, 1013-1021.
8. D. J. Berry and J. W. Steed, *Adv. Drug Delivery Rev.*, 2017, **117**, 3-24.
9. D. Haynes, W. Jones and W. Motherwell, *Crystengcomm*, 2005, **7**, 342-345.
10. CrysAlisPRO, Oxford Diffraction /Agilent Technologies UK Ltd, Yarnton, England.
11. G. M. Sheldrick, *Acta Crystallogr., Sect. A: Found. Crystallogr.*, 2008, **64**, 112-122.

12. O. V. Dolomanov, L. J. Bourhis, R. J. Gildea, J. A. K. Howard and H. Puschmann, *J. Appl. Crystallogr.*, 2009, **42**, 339-341.
13. A. A. Coehlo, *J. Appl. Crystallogr.*, 2018, **51**, 210-218.
14. A. Le Bail, H. Duroy and J. L. Fourquet, *Matt. Res. Bull.*, 1988, **23**, 447-452.
15. H. M. Rietveld, *J. Appl. Crystallogr.*, 1969, **2**, 65-71.
16. W. Sommer, J. Gottwald, D. E. Demco and H. W. Spiess, *J. Magn. Reson., Ser A*, 1995, **113**, 131-134.
17. I. Schnell, A. Lupulescu, S. Hafner, D. E. Demco and H. W. Spiess, *J. Magn. Reson.*, 1998, **133**, 61-69.
18. S. Cavadini, S. Antonijevic, A. Lupulescu and G. Bodenhausen, *J. Magn. Reson.*, 2006, **182**, 168-172.
19. S. Cavadini, *Prog. Nucl. Magn. Reson. Spectrosc.*, 2010, **56**, 46-77.
20. A. S. Tatton, J. P. Bradley, D. Iuga and S. P. Brown, *Z. Phys. Chem.*, 2012, **226**, 1187-1203.
21. Z. H. Gan, J. P. Amoureux and J. Trebosc, *Chem. Phys. Lett.*, 2007, **435**, 163-169.
22. M. H. Levitt, T. G. Oas and R. G. Griffin, *Isr. J. Chem.*, 1988, **28**, 271-282.
23. T. G. Oas, R. G. Griffin and M. H. Levitt, *J. Chem. Phys.*, 1988, **89**, 692-695.
24. D. Sakellariou, A. Lesage, P. Hodgkinson and L. Emsley, *Chem. Phys. Lett.*, 2000, **319**, 253-260.
25. B. Elena, G. de Paepe and L. Emsley, *Chem. Phys. Lett.*, 2004, **398**, 532-538.
26. B. M. Fung, A. K. Khitrin and K. Ermolaev, *J. Magn. Reson.*, 2000, **142**, 97-101.
27. G. Metz, X. L. Wu and S. O. Smith, *J. Magn. Reson., Ser A*, 1994, **110**, 219-227.
28. S. Hayashi and K. Hayamizu, *Bull. Chem. Soc. Jpn.*, 1991, **64**, 685-687.
29. C. R. Morcombe and K. W. Zilm, *J. Magn. Reson.*, 2003, **162**, 479-486.
30. S. Hayashi and K. Hayamizu, *Bull. Chem. Soc. Jpn.*, 1991, **64**, 688-690.
31. S. J. Clark, M. D. Segall, C. J. Pickard, P. J. Hasnip, M. J. Probert, K. Refson and M. C. Payne, *Z. Kristallogr.*, 2005, **220**, 567-570.
32. J. P. Perdew, K. Burke and M. Ernzerhof, *Phys. Rev. Lett.*, 1996, **77**, 3865-3868.
33. C. J. Pickard and F. Mauri, *Phys. Rev. B*, 2001, **63**, 245101.
34. J. R. Yates, T. N. Pham, C. J. Pickard, F. Mauri, A. M. Amado, A. Gil and S. P. Brown, *J. Am. Chem. Soc.*, 2005, **127**, 10216-10220.
35. A. C. Poppler, D. Walker and S. P. Brown, *CrystEngComm*, 2017, **19**, 224-236.
36. G. N. M. Reddy, D. S. Cook, D. Iuga, R. I. Walton, A. Marsh and S. P. Brown, *Solid State Nucl. Magn. Reson.*, 2015, **65**, 41-48.
37. R. K. Harris, P. Hodgkinson, C. J. Pickard, J. R. Yates and V. Zorin, *Magn. Reson. Chem.*, 2007, **45**, S174-S186.
38. T. Venâncio, L. M. Oliveira, J. Ellena, N. Boechat and S. P. Brown, *Solid State Nucl. Magn. Reson.*, 2017, **87**, 73-79.
39. F. M. Paruzzo, A. Hofstetter, F. Musil, S. De, M. Ceriotti and L. Emsley, *Nature Communications*, 2018, **9**, 4501.
40. J. D. Hartman, R. A. Kudla, G. M. Day, L. J. Mueller and G. J. O. Beran, *Phys. Chem. Chem. Phys.*, 2016, **18**, 21686-21709.
41. M. Zilka, S. Sturniolo, S. P. Brown and J. R. Yates, *J. Chem. Phys.*, 2017, **147**, 144203.
42. J. Bernstein, R. Davis, L. Shimoni and N. Chang, *Angew. Chem., Int. Ed.*, 1995, **34**, 1555-1573.
43. Y. Pan, Z. Jin, C. Sun and C. Jiang, *Chemistry Letters*, 2001, **30**, 1008-1009.
44. E. K. Corlett, H. Blade, L. P. Hughes, P. J. Sidebottom, D. Walker, R. I. Walton and S. P. Brown, *Crystengcomm*, 2019, **21**, 3502-3516.
45. D. A. Haynes, W. Jones and W. D. S. Motherwell, *Crystengcomm*, 2006, **8**, 830-840.
46. M. Hemamalini and H. Fun, *Acta Crystallographica Section E-Structure Reports Online*, 2010, **66**, O2093-U1847.
47. S. P. Brown, *Prog. Nucl. Magn. Reson. Spectrosc.*, 2007, **50**, 199-251.
48. S. P. Brown, in *Modern Methods in Solid-state NMR: A Practitioner's Guide*, ed. P. Hodgkinson, Royal Society of Chemistry, London, 2018, ch. 2, pp. 39-74.
49. A. C. Poppler, E. K. Corlett, H. Pearce, M. P. Seymour, M. Reid, M. G. Montgomery and S. P. Brown, *Acta Crystallogr., Sect. C: Cryst. Struct. Commun.*, 2017, **73**, 149-156.

50. L. Mafra, S. M. Santos, R. Siegel, I. Alves, F. A. A. Paz, D. Dudenko and H. W. Spiess, *J. Am. Chem. Soc.*, 2012, **134**, 71-74.
51. J. Schmidt, A. Hoffmann, H. W. Spiess and D. Sebastiani, *J. Phys. Chem. B*, 2006, **110**, 23204-23210.
52. C. Gervais, M. Profeta, V. Lafond, C. Bonhomme, T. Azaïs, H. Mutin, C. J. Pickard, F. Mauri and F. Babonneau, *Magn. Reson. Chem.*, 2004, **42**, 445-452.

TOC graphic